ADVANCED ENERGY MATERIALS
www.advenergymat.de

Photovoltaic Switching Mechanism in Lateral Structure Hybrid Perovskite Solar Cells

*Yongbo Yuan, Jungseok Chae, Yuchuan Shao, Qi Wang, Zhengguo Xiao, Andrea Centrone, and Jinsong Huang**

Organometal trihalide perovskite (OTP) materials have attracted broad attention due to their optical and electrical properties that are promising for solar cell applications.[1] In the past few years, the power conversion efficiency of OTP solar cells dramatically improved from 3.8% to a certified 20.1%.[2] Meanwhile, light-emitting devices and photodetectors with OTPs as the active material have also been demonstrated.[3] In contrast with the rocketing device efficiency, the understanding of how the fundamental material properties of OTPs are related to device operation is still limited.[1b,4] In an effort to understand the origin of photocurrent hysteresis, common in many OTP solar cells,[5] we recently discovered an intriguing switchable photovoltaic effect in both vertical and lateral structures devices.[6] By poling the methyl ammonium lead tri-iodide ($MAPbI_3$) layer sandwiched between two electrodes of the same material, (either either poly(3,4-ethylenedioxythiophene) polystyrene sulfonate, gold, nickel, platinum, or graphite) we showed that the direction of the diode polarity and the photocurrents in these devices could be reversed.[6] The poled solar cells showed a large short-circuit current (J_{SC}) of ≈20 mA cm^{-2} and a reasonable open-circuit voltage (V_{OC}) of ≈0.6 V in vertical structure devices.[6] The switchable OTP lateral device architecture can eliminate the biggest cost component of perovskite solar panels, i.e., the transparent electrodes required in the more common vertical structure devices, which could reduce the device cost significantly. However, to take full advantage of such architecture the crystallinity of the perovskite film should be optimized to match the charge diffusion length of the film with the electrode spacing. Moreover, lateral structure devices connected in series can output a photovoltage which is the sum of the photovoltage of each device (between 0.6 and 70 V for the devices studied here, **Figure 1**). This is an important characteristic because a higher voltage is needed in many applications, such as household devices (110 V), battery chargers (12 V), etc. However, the origin of the switching mechanism of the photovoltaic effect in OTP devices is unknown.

A switchable photovoltaic effect in lateral devices made by ferroelectric materials has been observed to be caused by "shift current" due to the asymmetric momentum distribution of photogenerated charge carriers,[7] or in materials with domain boundaries.[8] Nevertheless, the switchable photovoltaic effect observed in OTP devices cannot be explained as a "bulk photovoltaic effect" because of the independence V_{OC} with respect to the electrode spacing distance and because of the switching capability is reduced at low temperature.[6] We previously hypothesized that the electromigration of cations or anions could induce p and n doping in proximity of the two electrodes, thus forming a flipped p-i-n structure after poling the device with reversed bias, but direct evidence of ion electromigration has not been found yet. The verification of this hypothesis (i.e., ionic electromigration) in OTP devices is important because it can also provide clues for explaining the origin of the photocurrent hysteresis that plagues many OTP solar cell devices. In this paper, we report the direct observation of electromigration of methylammonium ions (MA^+) in $MAPbI_3$ perovskite films and the consequent formation of a p-i-n structure. The poling process and the dynamic of ions migration in $MAPbI_3$ film are also studied here at the macroscale.

The lateral structure OTP solar cells used in this work consist of a $MAPbI_3$ film between two gold (Au) electrodes that were deposited on top, as shown in Figure 1a. Au electrodes with spacing of 8, 50, or 100 µm were deposited on glass by thermal evaporation. The $MAPbI_3$ perovskite films were formed by the interdiffusion method where the methylammonium iodide (MAI) and lead iodide (PbI_2) stacked layers were thermally annealed at 100 °C for 1 h.[9] Figure 1b shows the photocurrent for a device with 8 µm electrode spacing before and after poling in different directions. As expected, the lateral device showed zero J_{sc} and V_{oc} before electrical poling (Figure 1b) because the electrodes, made with the same material (Au), do not induce preferential directionality (asymmetry) for charge transport. However, a photovoltaic effect was clearly observed after poling the device with a positive bias of 10 V (corresponding to an electric field of 1.25 V $µm^{-1}$) for approximately 90 s at room temperature. The lateral structure devices with 175 cells connected in series having the same poling direction can output V_{OC} as high as 70 V (Figure 1c).

To identify the mobile ions and verify the hypothesis that ions electromigration could induce doping in the perovskite film in proximity of the two electrodes, we first applied

Dr. Y. Yuan, Dr. Y. Shao, Dr. Q. Wang,
Dr. Z. Xiao, Prof. J. Huang
Department of Mechanical
and Materials Engineering
University of Nebraska-Lincoln
Lincoln, NE 68588-0656, USA
E-mail: jhuang2@unl.edu
Dr. J. Chae, Dr. A. Centrone
Center for Nanoscale Science and Technology
National Institute of Standards and Technology
100 Bureau Drive
Gaithersburg, MD 20899, USA
Dr. J. Chae
Maryland Nanocenter
University of Maryland
College Park, MD 20742, USA

DOI: 10.1002/aenm.201500615

ADVANCED ENERGY MATERIALS
www.advenergymat.de

www.MaterialsViews.com

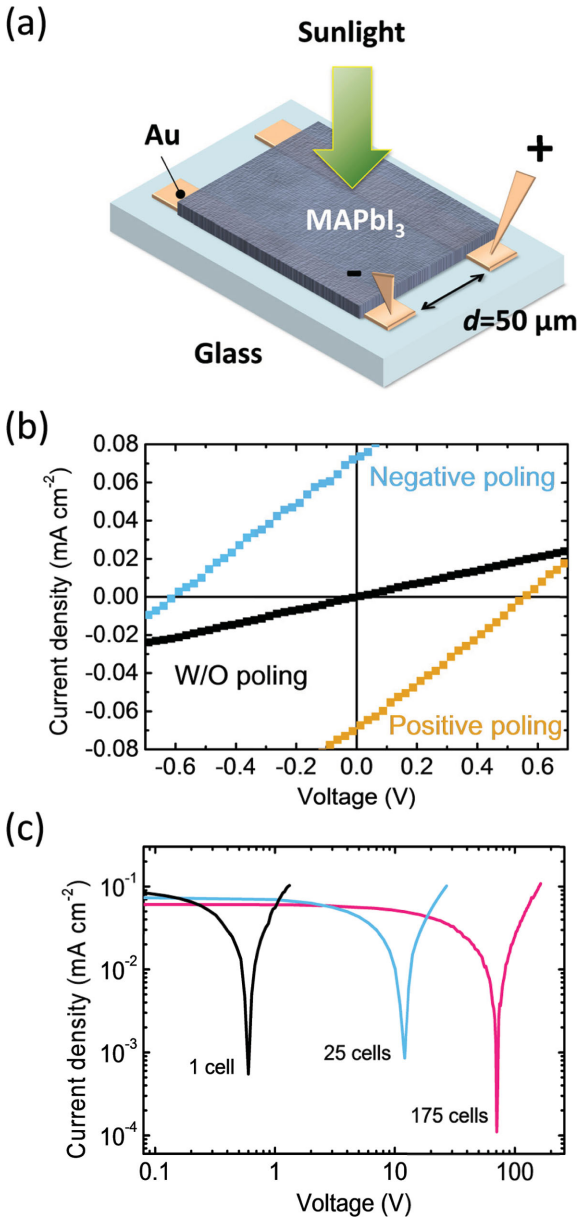

Figure 1. a) Configuration of the lateral perovskite solar cells; b) Current–voltage characteristics of lateral perovskite solar cell with electrode spacing of 8 μm before and after electrical poling (1.2 V μm^{-1} for 100 s), obtained with 25 mW cm^{-2} light intensity at a sweeping rate of ≈0.05 V s^{-1}. c) Current–voltage characteristics of series connected lateral devices after electrical poling, obtained in the same condition as in panel (b).

photothermal induced resonance (PTIR) microscopy,[10] a composition sensitive mapping technique, to map the spatial distribution of MA^+. Subsequently, we mapped the local surface electrical potential with Kelvin probe force microscopy (KPFM).[11] PTIR uses a pulsed wavelength-tunable IR laser for excitation and an atomic force microscopy (AFM) tip operating in contact mode as a local detector (**Figure 2**a) of IR spectra and maps with a resolution as high as 20 nm,[12] much beyond the optical diffraction limit. The function of the AFM tip is to transduce locally the sample thermal expansion, due to light absorption, into large cantilever oscillations which are detected in the far-field by reflecting a diode laser into the AFM four-quadrant detector. Because of the specificity of IR spectroscopy to the chemical composition, PTIR allows mapping the distribution of given chemical species (or chemical groups), and has enabled the characterization of diverse samples including: plasmonic nanomaterials,[13] metal-organic frameworks,[14] polymers[10d,15] and, very recently, OTPs.[3b] In this work, the PTIR technique is used to map the distribution of the MA^+ before and after electrical poling. To enable PTIR characterization, a perovskite lateral device was fabricated on the surface of a zinc selenide prism. The prism is used to illuminate the sample in total internal reflection thus minimizing the light-tip direct interaction. The PTIR data were recorded under a dry nitrogen flow using a custom built enclosure which also allows to electrically pole the OTP films *in situ*. A representative PTIR spectra from the OTP film is reported in Figure 2b showing the IR absorption peaks of MA^+. The vibrational modes involving Pb ions occur at much lower frequencies and are outside the spectral range of our PTIR setup.[12] The AFM topography image and the PTIR image of CH_3 asymmetric deformation of the methylammonium ion (1468 cm^{-1}) obtained before electrical poling show that the OTP device is fairly homogeneous and that the distribution of MA^+ ions is uniform (Figure 2c,d). The bright line along the Au electrode edge in the PTIR map is caused by the plasmonic enhancement of PTIR signal induced by the gold electrode. The topography images obtained after electrical poling with an electric field of 1.6 V μm^{-1} for 100 s (Figure 2e) and 200 s (Figure 2g) do not show significant changes. In contrast, the corresponding PTIR chemical maps (Figure 2f,h) show that the MA^+ absorption intensity become stronger in proximity of the cathode as a function of the poling time. Since for thin samples (<1 μm) the PTIR signal is proportional to the absorbed energy,[10b] under the assumption that the IR absorption cross section of MA^+ is constant, the PTIR maps indicate redistribution in the concentration of the MA^+ under electrical poling. These maps provide direct evidence of the electromigration of the MA^+ ions towards the negatively charge electrode. Line profiles of the PTIR signal intensity before and after electrical poling are reported in Figure 2i, showing that the accumulation of the MA^+ ions extends for ≈10 μm in proximity of the cathode. Conversely a depletion of MA^+ from center to the anode side is also observed. This is the first time that the electromigration of MA^+ is directly observed in a $MAPbI_3$ film and effectively supports our hypothesis.

The facile MA^+ electromigration can be related to the material structure. It is known that in $MAPbI_3$ the MA groups occupy the A sites of the perovskite structure.[16] It has been observed experimentally and theoretically that the MA group exhibits a fast rotational dynamics within the inorganic framework with a relaxation time of few ps at room temperature,[16b,17] suggesting a relatively weak and nondirectional ionic bonding between MA^+ and the inorganic framework.[5d] It should be noted that electromigration of Pb^{2+} or I^- could also potentially cause the activation of the photovoltaic effect in OTP films. Although, no redistribution of Pb^{2+} or I^- in the lateral structure devices was observed by us using energy-dispersive X-ray spectroscopy (EDS) in the same poling conditions (Figure S1, Supporting Information), the electromigration of such ions cannot be excluded because of the limited detectivity of EDS.

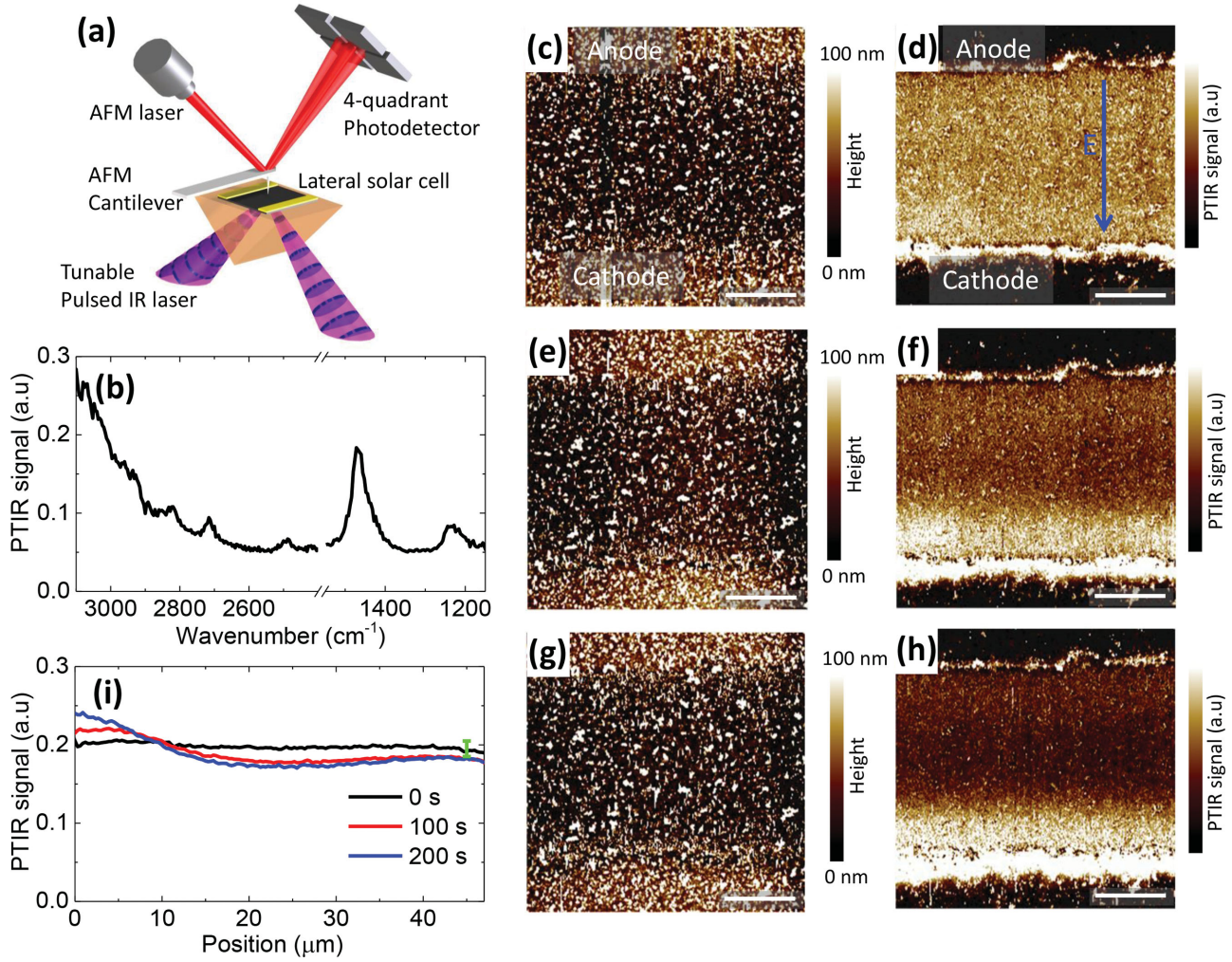

Figure 2. a) Schematic illustration of the PTIR measurement. b) A representative absorption spectrum obtained at the center of the device. c,e,g) Topography maps (80 μm × 80 μm) of the $MAPbI_3$ film of the same sample area before (c), after 100 s (e) and after 200 s (g) electrical poling, respectively. The poling field was 1.6 V μm^{-1}. d,f,h) Corresponding PTIR images for the CH_3 asymmetric deformation absorption of the methylammonium ion (1468 cm^{-1}) obtained before (d), after 100 s (f) and after 200 s (h) electrical poling, respectively. i) Line-averaged profile (perovskite region only) of 256 vertical lines in the PTIR images before and after electrical poling, showing the redistribution of the MA^+ ions. The error bar represents the uncertainty of the background level when comparing data from different scans. All scale bars are 20 μm.

Since the MA^+ ions themselves do not participate in the formation of valence and conduction bands of the perovskite,[18] MA^+ does not provide doping directly. Previous theoretical calculation predicts that the accumulation of the MA^+ vacancy ($V_{MA}^{\bullet}$) in proximity of the anode should results in p-type doping of the $MAPbI_3$ film by attracting holes to maintain charge neutrality in the film.[19] Similarly, the accumulation of MA^+ ions near the cathode is expected to induce n-type doping. To confirm that the redistribution of MA^+ ions induces doping in the $MAPbI_3$ film we applied KPFM to identify changes of the surface work function induced by poling in the lateral structure devices. KPFM is a scanning probe technique that can provide maps of the local surface electrical potential or work function with a spatial resolution of tens of nm.[11b] The schematic of the KPFM experiments is shown in **Figure 3**a. Doping of a material induces a change of surface work function, which can be detected in the KPFM measurement. This effect is illustrated in Figure 3d with the energy diagrams of the device before and after the poling process. The lateral structure device used here avoids possible chemical contamination that could be induced by the top electrode in vertical structure devices.[4b,20] The KPFM tip was scanned 80 nm above the perovskite film, covering a 30 μm × 15 μm area between the two electrodes (that are spaced 50 μm apart). Similarly to what observed in the PTIR experiments, the unpoled $MAPbI_3$ film show a uniform surface potential throughout the whole scanning region (Figure 3b), confirming the film uniformity. In striking contrast, the surface potential distribution of the poled (1.2 V μm^{-1}, for 100 s) $MAPbI_3$ film increases gradually from the region in proximity of the cathode (right side) to the region in proximity of the anode (left side) (Figure 3c). Such gradual increase is in agreement with the assumption of p-doping occurring in proximity of the anode. The work function changes by ≈0.35 V in the 30-μm-long probed region which is reasonable, considering

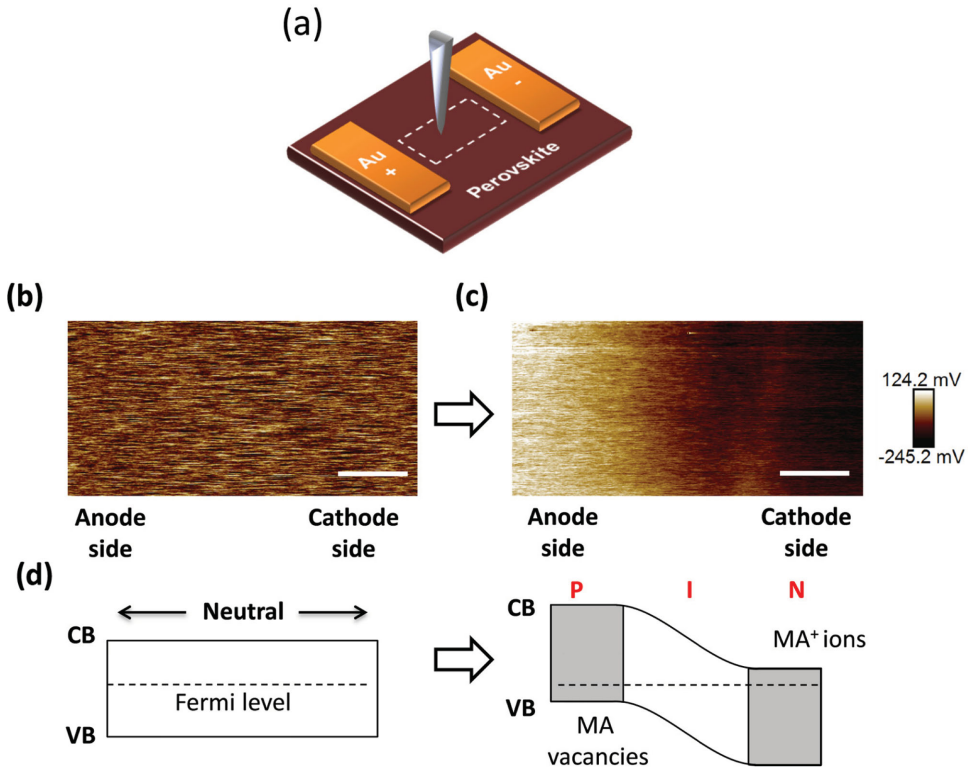

Figure 3. a) Schematic of the KPFM measurements of the lateral structure devices, where the white dash line indicates the location of the scanning region. b,c) KPFM potential images of the $MAPbI_3$ thin films between the two Au electrodes before (b) and after (c) electrical poling (1.2 V μm^{-1} for 100 s), respectively. The electrode spacing is 50 μm. The scale bar is 6 μm; d) energy diagram of the $MAPbI_3$ film before and after electrical poling, where p-i-n junction was formed due to the accumulation of MA^+ ions (vacancies) in proximity of the cathode (anode) side.

that the lateral cell with an electrode spacing of 50 μm has a V_{OC} output of 0.6 V. Poling the lateral device with positive bias gives a positive V_{OC} and negative J_{SC} (Figure 3d), which is consistent with the results in Figure 1b. This finding suggests that electrical properties of the $MAPbI_3$ film can be manipulated after the film fabrication by applying an electric field, which is a convenient and potentially widely applicable method for designing novel OTP optoelectronic devices.

Having established that the electromigration of MA^+ ions is the driving mechanism of the switchable photovoltaic effect, we further investigate the electromigration process at the macroscopic level. The electromigration rate was quantified by monitoring the switching process in the lateral device with a larger electrode spacing of 50 μm to intentionally increase the electromigration distance. **Figure 4**a shows the flipping process of a previously poled lateral device obtained by repeatedly applying electric field pulses (1.5 V μm^{-1}, for 10 s) to the device, followed by a current–voltage (*I*–*V*) measurement. Ion migration that may be induced during the *I*–*V* measurement (from −2 to 2 V) is negligible because the large electrode spacing makes the applied electric field (0.04 V μm^{-1}) much smaller than the poling electric field (1.5 V μm^{-1}). As shown in Figure 4a, the V_{OC} and J_{SC} change gradually under an electrical field of 1.5 V μm^{-1}, as a result of the ion migration occurring over a distance of tens of micrometers. The V_{OC} of this device saturates at ≈0.62 V which is close to V_{OC} measured for the devices with 8 μm electrode spacing. Approximately 120 ± 20 s are necessary for flipping the device from one polarization state to the other, implying an ion mobility (μ) of $1.5 \times 10^{-9} \pm 0.5 \times 10^{-9}$ cm^2 Vs^{-1}, where the μ is defined as the ratio between the ion drifting velocity (v) and electrical field ($\mu = E/v$). The ion mobility of the $MAPbI_3$ film is large and in vertical structure devices, MA^+ ions could drift from side to side in few seconds because of the small distance (≈300 nm) between the electrodes.[6]

For a better understanding of the MA^+ electromigration, we subjected lateral $MAPbI_3$ devices to different poling electric fields and temperatures (Figure 4b). At each temperature, the device was poled with different electric fields for 60 s, followed by *I*–*V* curve scanning to measure the device V_{OC}. At room temperature, V_{OC} increased rapidly when the poling electrical field was increased from 0.1 V μm^{-1} to 0.5 V μm^{-1} and saturated when the electric field exceeded 1.0 V μm^{-1}. This result clearly shows that, at room temperature, the MA^+ in $MAPbI_3$ film can readily move under an applied electrical field as small as ≈0.3 V μm^{-1}, which is considerably smaller than the electric field induced by the photovoltage in many vertical $MAPbI_3$ perovskite solar cells (≈3 V μm^{-1}).[21] Consequently it is likely that the photovoltage generated during OTP solar cell operation may be sufficient to induce the electromigration of MA^+ in $MAPbI_3$ films, possibly impacting the device efficiency, photocurrent hysteresis behavior and stability, although the film morphology in other devices may differ from the one observed here. The poling process become more difficult when the temperature decreased from room temperature to 250 K, i.e., a larger electrical field is required to reach a same V_{OC} value at lower temperature, which is typical of ion migration. The poling process can

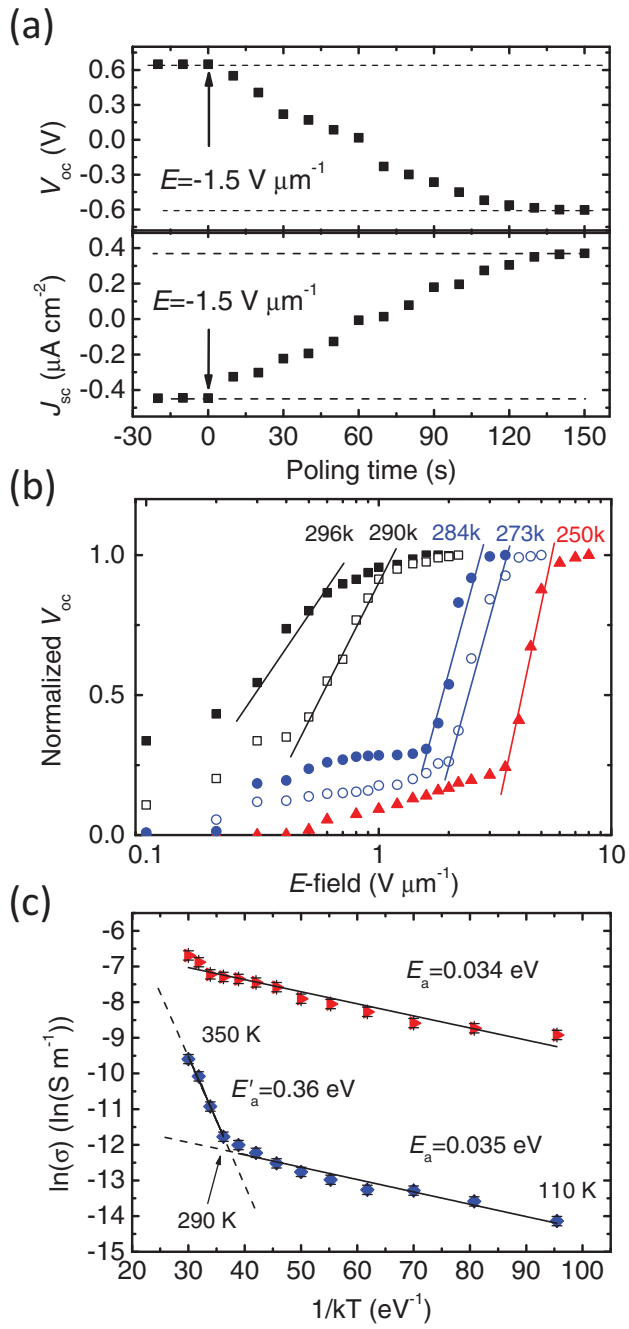

Figure 4. a) Flipping of V_{OC} and J_{SC} obtained when applying an electrical field of 1.5 V μm^{-1} on OTP devices with different poling times; b) V_{OC} values as a function of temperature obtained for lateral devices, poled for 60 s; c) Arrhenius plot of the conductivity of the $MAPbI_3$ film under dark (blue) and illumination (red, the light intensity is 0.25 mW cm^{-2}). The error bars represent a single standard deviation in the calculation of the sample conductivity and are mainly determined by the uncertainty in the current measured in the experiments.

be divided into two stages: in the first stage, the V_{OC} increases gradually from zero to ≈20% to ≈40% (sample dependent) of its maximum value under a relatively small electrical field; in the second stage, the V_{OC} increases to the V_{OC} saturation value for relatively large electric fields. Hereafter, we refer to as "fast-ions" the ions responsible for the first stage, and as "slow-ions" the ions responsible for the second stage. The V_{OC} value for which the transition from the first to the second stage is observed varied from batch to batch. We tentatively attribute such variability to the different relative amount of "fast-ions" in deposited $MAPbI_3$ films. For the "slow-ions" the onset electrical field necessary to induce ion migration increases from 0.3 V μm^{-1} at room temperature to 3 V μm^{-1} at 250 K; clearly indicating that the "slow-ion" migration requires a larger activation energy. The origins of the "fast-ions" and "slow-ions" have not been identified yet. Perhaps they represent MA^+ ions moving through different "channels," e.g., on the film surface/grain boundaries or through the bulk of the $MAPbI_3$ crystals.

The activation energy (E_a) for the ion migration was determined by measuring the conductivity (σ) changes of $MAPbI_3$ films under 0.35 V μm^{-1} electrical field at different temperatures (see the Arrhenius plot in Figure 4c).[22] Since the conductivity of the $MAPbI_3$ film may arise from both charge carriers and mobile ions, we can discriminate their contributions by examining the dark and photo conductivity of the films. Under illumination, the photogenerated electron/holes should be the dominant contribution to the conductivity (photoconductivity) and also partially screen the electric field applied to the ions. Figure 4c plots the lateral conductivity of 250 nm thick $MAPbI_3$ film in darkness (blue) and under illumination (0.25 mW cm^{-2}, red). In the dark, the $\ln(\sigma) - 1/kT$ curve consists of two linear regions: the first linear region (from 100 K to 270 K) shows an E_a of 35 meV ± 3 meV; the second linear region (from 290 K to 350 K) shows a tenfold larger E_a of 360 meV ± 19 meV. The uncertainties in the activation energy represent a single standard deviation in the fitting of the Arrhenius plot. The smaller activation energy region is assigned to the charge carrier transport in $MAPbI_3$ films, which practically coincides with the activation energy obtained from the photoconductivity under illumination (34 meV ± 3 meV). First-principles calculations done by Yin and others predicted that defects with low formation energy in α-phase $MAPbI_3$ crystal, such as Pb vacancies, I interstitial, or MA interstitial, form shallow traps with depth smaller than 50 meV.[19a] Therefore assigning the smaller E_a (≈35 meV) to charge carrier transport is reasonable. The larger activation energy of ≈360 meV, observed in the dark, is assigned to the electromigration of MA^+. Compared to carrier charge conduction, electromigration dominates the conductivity only at relatively high temperature (310–350 K) because of its large activation energy. The transition occurs around room temperature (290 K), where the ionic conduction only contributes slightly to the total conduction. The high ionic conductivity imposes another challenge for the use of OTP materials in solar cell applications because of the higher solar panel temperatures observed in operating conditions. The activation energy for MA^+ migration in $MAPbI_3$ film (≈360 meV) is comparable to those observed in other perovskite halide films such as $CsPbBr_3$ (250 meV) and $CsPbCl_3$ (290 meV).[22] Interestingly, the E_a value of MA^+ electromigration is also close to the formation energy of the MA^+ substitutions in I-rich perovskites (MA_{Pb}, 280 meV) or for MA^+ interstitials in I-poor perovskites (MA_i, 200 meV), implying the possible route for the MA^+ ion migration inside the $MAPbI_3$ crystal, i.e., the MA^+ may migrate by substituting Pb or via MA^+ interstitial sites.[19a]

In summary, the ionic electromigration has been identified as the origin of the switchable photovoltaic effect in $MAPbI_3$ perovskite lateral structure devices. The electromigration and redistribution of MA^+ ions at room temperature was directly observed for the first time with PTIR measurements. KPFM maps show that a p-i-n structure was generated in the center region of poled lateral devices. Electrical measurements show that the MA^+ can readily migrate when subjected to an electric field as small as ≈0.3 V μm^{-1} at room temperature. The ion migration mobility is estimated to be ≈1.5 × 10^{-9} cm^2 Vs^{-1} at 1.5 V μm^{-1}. The ionic conduction in the $MAPbI_3$ film is contributed by both "fast ions" and "slow ions." The activation energy of "fast ions" is 360 meV ± 19 meV. This study provides new insights for understanding $MAPbI_3$ properties and provides a novel method for manipulating the electric properties of $MAPbI_3$ film.

Experimental Section

Device Fabrication: 75 nm thick Au electrode with spacing of 8, 50, or 100 μm was thermally deposited on glass substrates by photolithography or using shadow mask. Subsequently a $MAPbI_3$ film, with a thickness of ≈300 nm, was spin coated with the interdiffusion method. PbI_2 (40%, g g^{-1}) and MAI (4.0%, g g^{-1}) were first dissolved in dimethylformamide and 2-propanol, respectively, to form precursor solutions. The PbI_2 hot solution was spun onto glass at 100 Hz. Then the hot MAI solution was spin coated on PbI_2 film at 100 Hz for 35 s. The bilayer films were then annealed at 100 °C for 1 h.

Film and Device Characterization: Measurements on lateral solar cells were conducted in a probe station chamber under a vacuum of 10^{-5} Pa, with white light (25 mW cm^{-2}) through a quartz window. A high voltage supply with a maximum voltage output of 1200 V was used for the poling process. Here, positive (negative) poling is defined for positive (negative) applied bias to the lateral solar cell. A semiconductor analyzer was used for the current–voltage characterization. KPFM and AFM measurements were carried out in air and in the dark. Platinum–iridium-coated conductive probes were used in the KPFM and AFM measurements. The peak force KPFM mode, combining the tapping mode AFM with frequency modulation KPFM was used to measure the topographic and surface potential signals from the same sample area. The scanning area and tip velocity were 30 μm × 15 μm and 81.4 μm s^{-1}, respectively. The lift height for KPFM measurements was 80 nm for all samples. The conductivity of the $MAPbI_3$ film was measured at different temperatures with a semiconductor analyzer, by applying 35 V bias to devices with electrode spacing of 100 μm, corresponding to an average electrical field of 0.35 V μm^{-1}. To avoid transient current spikes which occurred in the first few seconds after bias, the conductivity was extracted from the device current between 10 and 40 s after the bias was applied. In order to avoid a possible heating effect on the perovskite film caused by light illumination a relative weak light intensity of 0.25 mW cm^{-2} was used in the experiments.

PTIR Characterization: PTIR experiments were carried out using a commercial PTIR setup that consists of an AFM microscope operating in contact mode and a tunable pulsed laser source consisting of an optical parametric oscillator based on a noncritically phase-matched $ZnGeP_2$ crystal. The laser emits pulses 10 ns long at 1 kHz repetition rate that are tunable from 4000 cm^{-1} to ≈1025 cm^{-1} (from 2.5 μm to 9.76 μm). The low repetition rate of the laser (1 kHz) assures that a new pulse will excite a sample and cantilever after they have returned to equilibrium. The typical laser spot size is ≈30 μm at the sample. PTIR experiments were obtained by flowing nitrogen gas (0.12 dm^3 s^{-1}) in custom enclosure built around the sample.

$MAPbI_3$ samples for PTIR analysis were fabricated according to the procedure described above directly on a zinc selenide right angle prism coated by a thin layer of poly(3,4-ethylenedioxythiophene) polystyrene sulfonate at a frequency of 100 Hz using a custom spinner adaptor. A source measure unit was used for electrical poling by applying a voltage of 75 V between two Au electrodes (spaced by 47 μm).

PTIR spectra were obtained by averaging the cantilever deflection amplitude from 256 individual laser pulses at each wavelength and tuning the laser at intervals of 4 cm^{-1}. PTIR images were recorded by illuminating the sample with a constant wavelength while scanning the AFM tip. The AFM height and the PTIR signal acquisition was synchronized so that for each AFM pixel the PTIR signal is an average over 32 laser pulses. The pixel sizes are 300 nm × 300 nm in all images. Commercially available 450 μm long silicon contact-mode AFM probes with a nominal spring constant between 0.07 N m^{-1} and 0.4 N m^{-1} were used for this study.

Supporting Information

Supporting Information is available from the Wiley Online Library or from the author.

Acknowledgements

J.H. thanks financial support from National Science Foundation under Awards ECCS-1252623, Department of Energy under Award DE-EE0006709, and the Nebraska Public Power District through the Nebraska Center for Energy Sciences Research. J.C. acknowledges support under the Cooperative Research Agreement between the University of Maryland and the National Institute of Standards and Technology Center for Nanoscale Science and Technology, Award 70NANB10H193, through the University of Maryland.

Received: March 25, 2015
Revised: May 6, 2015
Published online:

[1] a) H. J. Snaith, *J. Phys. Chem. Lett.* **2013**, *4*, 3623; b) H. S. Jung, N. G. Park, *Small* **2015**, *11*, 10; c) M. A. Green, A. Ho-Baillie, H. J. Snaith, *Nat. Photonics* **2014**, *8*, 506; d) W.-J. Yin, J.-H. Yang, J. Kang, Y. Yan, S.-H. Wei, *J. Mater. Chem. A* **2015**, *3*, 8926 e) Q. Dong, Y. Fang, Y. Shao, P. Mulligan, J. Qiu, L. Cao, J. Huang, *Science* **2015**, 967.

[2] N. J. Jeon, J. H. Noh, W. S. Yang, Y. C. Kim, S. Ryu, J. Seo, S. I. Seok, *Nature* **2015**, *517*, 476.

[3] a) Z.-K. Tan, R. S. Moghaddam, M. L. Lai, P. Docampo, R. Higler, F. Deschler, M. Price, A. Sadhanala, L. M. Pazos, D. Credgington, *Nat. Nanotechnol.* **2014**, *9*, 687; b) R. Dong, Y. Fang, J. Chae, J. Dai, Z. Xiao, Q. Dong, Y. Yuan, A. Centrone, X. C. Zeng, J. Huang, *Adv. Mater.* **2015**, *27*, 1912; c) L. Dou, Y. M. Yang, J. You, Z. Hong, W.-H. Chang, G. Li, Y. Yang, *Nat. Commun.* **2014**, *5*, 5404; d) Y. Fang, J. Huang, *Adv. Mater.* **2015**, *27*, 2804.

[4] a) D. A. Egger, E. Edri, D. Cahen, G. Hodes, *J. Phys. Chem. Lett.* **2015**, *6*, 279; b) G. Niu, X. Guo, L. Wang, *J. Mater. Chem. A* **2015**, *3*, 8970.

[5] a) H. J. Snaith, A. Abate, J. M. Ball, G. E. Eperon, T. Leijtens, N. K. Noel, S. D. Stranks, J. T.-W. Wang, K. Wojciechowski, W. Zhang, *J. Phys. Chem. Lett.* **2014**, *5*, 1511; b) E. Unger, E. Hoke, C. Bailie, W. Nguyen, A. Bowring, T. Heumüller, M. Christoforo, M. McGehee, *Energy Environ. Sci.* **2014**, *7*, 3690; c) Y. Shao, Z. Xiao, C. Bi, Y. Yuan, J. Huang, *Nat. Commun.* **2014**, *5*, 5784; d) J. M. Frost, K. T. Butler, A. Walsh, *APL Mater.* **2014**, *2*, 081506; e) H.-S. Kim, N.-G. Park, *J. Phys. Chem. Lett.* **2014**, *5*, 2927; f) J. Wei, Y. Zhao, H. Li, G. Li, J. Pan, D. Xu, Q. Zhao, D. Yu, *J. Phys. Chem. Lett.* **2014**, *5*, 3937.

[6] Z. Xiao, Y. Yuan, Y. Shao, Q. Wang, Q. Dong, C. Bi, P. Sharma, A. Gruverman, J. Huang, *Nat. Mater.* **2015**, *14*, 193.

[7] a) A. Glass, D. Von der Linde, T. Negran, *Appl. Phys. Lett.* **1974**, *25*, 233; b) K. Yao, B. K. Gan, M. Chen, S. Shannigrahi, *Appl. Phys. Lett.* **2005**, *87*, 212906; c) Y. Yuan, Z. Xiao, B. Yang, J. Huang, *J. Mater. Chem. A* **2014**, *2*, 6027.

[8] S. Yang, J. Seidel, S. Byrnes, P. Shafer, C.-H. Yang, M. Rossell, P. Yu, Y.-H. Chu, J. Scott, J. Ager, *Nat. Nanotechnol.* **2010**, *5*, 143.

[9] a) Z. Xiao, C. Bi, Y. Shao, Q. Dong, Q. Wang, Y. Yuan, C. Wang, Y. Gao, J. Huang, *Energy Environ. Sci.* **2014**, *7*, 2619; b) C. Bi, Y. Shao, Y. Yuan, Z. Xiao, C. Wang, Y. Gao, J. Huang, *J. Mater. Chem. A* **2014**, *2*, 18508.

[10] a) A. Dazzi, R. Prazeres, F. Glotin, J. Ortega, *Opt. Lett.* **2005**, *30*, 2388; b) B. Lahiri, G. Holland, A. Centrone, *Small* **2013**, *9*, 439; c) A. M. Katzenmeyer, V. Aksyuk, A. Centrone, *Anal. Chem.* **2013**, *85*, 1972; d) J. R. Felts, K. Kjoller, M. Lo, C. B. Prater, W. P. King, *ACS Nano* **2012**, *6*, 8015; e) A. Centrone, *Annu. Rev. Anal. Chem.* **2015**, DOI: 10.1146/annurev-anchem-071114-40435.

[11] a) V. W. Bergmann, S. A. Weber, F. J. Ramos, M. K. Nazeeruddin, M. Grätzel, D. Li, A. L. Domanski, I. Lieberwirth, S. Ahmad, R. Berger, *Nat. Commun.* **2014**, *5*, 5001; b) U. Zerweck, C. Loppacher, T. Otto, S. Grafström, L. M. Eng, *Phys. Rev. B* **2005**, *71*, 125424.

[12] A. M. Katzenmeyer, G. Holland, K. Kjoller, A. Centrone, *Anal. Chem.* **2015**, *87*, 3154.

[13] a) B. Lahiri, G. Holland, V. Aksyuk, A. Centrone, *Nano lett.* **2013**, *13*, 3218; b) A. M. Katzenmeyer, J. Chae, R. Kasica, G. Holland, B. Lahiri, A. Centrone, *Adv. Opt. Mater.* **2014**, *2*, 718.

[14] A. M. Katzenmeyer, J. Canivet, G. Holland, D. Farrusseng, A. Centrone, *Angew. Chem. Int. Ed.* **2014**, *53*, 2852.

[15] Z. Cui, C. Coletta, A. Dazzi, P. Lefrancois, M. Gervais, S. Néron, S. Remita, *Langmuir* **2014**, *30*, 14086.

[16] a) A. Filippetti, A. Mattoni, *Phys. Rev. B* **2014**, *89*, 125203; b) J. M. Frost, K. T. Butler, F. Brivio, C. H. Hendon, M. van Schilfgaarde, A. Walsh, *Nano lett.* **2014**, *14*, 2584.

[17] a) E. Mosconi, C. Quarti, T. Ivanovska, G. Ruani, F. De Angelis, *Phys. Chem. Chem. Phys.* **2014**, *16*, 16137; b) A. Poglitsch, D. Weber, *J. Chem. Phys.* **1987**, *87*, 6373; c) C. Quarti, G. Grancini, E. Mosconi, P. Bruno, J. M. Ball, M. M. Lee, H. J. Snaith, A. Petrozza, F. D. Angelis, *J. Phys. Chem. Lett.* **2013**, *5*, 279; d) F. Brivio, A. B. Walker, A. Walsh, *APL Mater.* **2013**, *1*, 042111; e) Y. Wang, T. Gould, J. F. Dobson, H. Zhang, H. Yang, X. Yao, H. Zhao, *Phys. Chem. Chem. Phys.* **2014**, *16*, 1424.

[18] T. Umebayashi, K. Asai, T. Kondo, A. Nakao, *Phys. Rev. B* **2003**, *67*, 155405.

[19] a) W.-J. Yin, T. Shi, Y. Yan, *Appl. Phys. Lett.* **2014**, *104*, 063903; b) J. Kim, S.-H. Lee, J. H. Lee, K.-H. Hong, *J. Phys. Chem. Lett.* **2014**, *5*, 1312; c) Q. Wang, Y. Shao, H. Xie, L. Lyu, X. Liu, Y. Gao, J. Huang, *Appl. Phys. Lett.* **2014**, *105*, 163508.

[20] P. Peumans, S. Forrest, *Appl. Phys. Lett.* **2001**, *79*, 126.

[21] J. Shi, X. Xu, D. Li, Q. Meng, *Small* **2015**, DOI: 10.1002/smll.201403534.

[22] J. Mizusaki, K. Arai, K. Fueki, *Solid State Ionics* **1983**, *11*, 203.